

Extension of the entropy viscosity method to the low Mach regime for the multi-D Euler equations (with variable area).

Marc O. Delchini^a, Jean C. Ragusa^{*,a}, Ray A. Berry^b

^a*Department of Nuclear Engineering, Texas A&M University, College Station, TX 77843, USA*

^b*Idaho National Laboratory, Idaho Falls, ID 83415, USA*

Abstract

The entropy viscosity method, introduced by Guermond et al. [1, 2], is applied to the multi-D Euler equations with variable area for subsonic and supersonic flows. The entropy minimum principle is used to derive the dissipative terms for the multi-D Euler equations with variable area on the model of [3]. It is also shown that the current definition of the viscosity coefficients ([1]) is unadapted to subsonic flow and thus requires a fix. A low Mach asymptotic study is performed to derive a new definition for the viscosity coefficients that are well-scaled in the low Mach regime. Multiple 1- and 2-D tests are run with the Ideal and Stiffened Gas equation of state: flow in a convergent-divergent nozzle, Leblanc shock tube, subsonic flow over a 2-D cylinder and circular hump, and supersonic flow in a compression corner. These tests allow to validate our new approach. Convergence studies are performed when an analytical solution is available for the 1-D case.

Key words: Euler equations with variable area, entropy viscosity method, stabilization method, low Mach regime, shocks.

1. Introduction

Over the past years an increasing interest raised for computational methods that can solve both compressible and incompressible flows. In engineering applications, there is often the need to solve for complex flows where a near incompressible regime or low Mach flow coexists with a supersonic flow domain. For example, such flow are encountered in aerodynamic in the study of airships. In the nuclear industry, flows are nearly the incompressible regime but compressible effects cannot be neglected because of the heat source and thus needs

*Corresponding author

Email addresses: `delchmo@tamu.edu` (Marc O. Delchini), `jean.ragusa@tamu.edu` (Jean C. Ragusa), `ray.berry@inl.gov` (Ray A. Berry)

9 to be accurately resolved.
 10 When solving the multi-D Euler equations for a wide range of Mach numbers,
 11 multiple problems have to address: stability, accuracy and acceleration of the
 12 convergence in the low Mach regime. Because of the hyperbolic nature of the
 13 equations, shocks can form during transonic and supersonic flows, and require
 14 the use of the numerical methods in order to stabilize the scheme and cor-
 15 rectly resolve the discontinuities. The literature offers a wide range of stabiliza-
 16 tion methods: flux-limiter [4, 5], pressure-based viscosity method ([6]), Lapidus
 17 method ([7, 8, 9]), and the entropy-viscosity method([1, 2]) among others. These
 18 numerical methods are usually developed using simple equation of states and
 19 tested for transonic and supersonic flows where the disparity between the acous-
 20 tic waves and the fluid speed is not large since the Mach number is of order one.
 21 This approach leads to a well-known accuracy problem in the low Mach regime
 22 where the fluid velocity is smaller than the speed of sound by multiple order of
 23 magnitude. The numerical dissipative terms become ill-scaled in the low Mach
 24 regime and lead to the wrong numerical solution by changing the nature of the
 25 equations solved. This behavior is well documented in the literature [10, 11, 12]
 26 and often treated by performing a low Mach asymptotic study of the multi-D
 27 Euler equation. This method was originally used [10] to show convergence of
 28 the compressible multi-D Euler equations to the incompressible ones. Thus,
 29 by using the same method, the effect of the dissipative terms in the low Mach
 30 regime, can be understood and, when needed, a fix is developed in order to
 31 ensure the convergence of the equations to the correct physical solution. This
 32 approach was used as a fixing method for multiple well known stabilization
 33 methods alike Roe scheme ([13]) and SUPG [12] while preserving the original
 34 stabilization properties of shocks.
 35 We propose, through this paper, to investigate how the entropy viscosity method,
 36 when applied to the multi-D Euler equations with variable area, behaves in the
 37 low Mach regime. This method was initially introduced by Guermond et al.
 38 to solve for the hyperbolic systems and has shown good results when used for
 39 solving the multi-D Euler equations with various discretization schemes. More
 40 importantly, it is simple to implement, can be used with unstructured grids,
 41 and its dissipative terms are consistent with the entropy minimum principle
 42 and proven valid for any equation of state under certain conditions [3].
 43 This paper is organized as follows: in Section 2 the current definition of the en-
 44 tropy viscosity method is recalled, and inconsistency with the low Mach regime
 45 are pointed out. Since our interest is in the variable area version of the multi-D
 46 Euler equation, the reader is guided through the steps leading to the derivation
 47 of the dissipative terms on the model of [3]. Then in Section 3, a new definition
 48 of the viscosity coefficient is introduced and derived from a low Mach asymp-
 49 totic study. After detailing the spatial and temporal discretization method in
 50 Section 4, 1- and 2-D numerical results are presented in Section 5 for a wide
 51 range of Mach numbers: low Mach flow over a cylinder and a circular bump,
 52 and supersonic flow in a compression corner [14]. Convergence studies are per-
 53 formed in 1-D, in order to demonstrate the accuracy of the solution.
 54 For purpose of clarity, the multi-D Euler equations with variable area are re-

55 called in Eq. (1) and the corresponding variables are defined:

$$\begin{cases} \partial_t (\rho A) + \vec{\nabla} \cdot (\rho \vec{u} A) = 0 \\ \partial_t (\rho \vec{u} A) + \vec{\nabla} \cdot [(\rho \vec{u} \otimes \vec{u} + P \mathbf{I}) A] = P \vec{\nabla} A \\ \partial_t (\rho E A) + \vec{\nabla} \cdot [\vec{u} (\rho E + P) A] = 0 \\ P = P(\rho, e) \end{cases} \quad (1)$$

56 where ρ , $\rho \vec{u}$ and ρE are the density, the momentum and the total energy, re-
 57 spectively, and will be referred to as the conservative variables. The pressure
 58 P is computed with an equation of state expressed in function of the density ρ
 59 and the specific internal energy e . The tensor product $\vec{a} \otimes \vec{b}$ is taken with the
 60 following convention: $(\vec{a} \otimes \vec{b})_{i,j} = a_i b_j$. Lastly, the terms ∂_t , $\vec{\nabla}$, $\vec{\nabla} \cdot$ and \mathbf{I} denote
 61 the temporal derivative, the gradient and divergent operators, and the identity
 62 tensor, respectively. The variable area A is assumed spatial dependent.

63 2. The Entropy Viscosity Method

64 2.1. Background

65 In this section, the entropy-based viscosity method [1, 2, 15] is recalled for
 66 the multi-D Euler equations (with constant area A) [16]. The entropy-based
 67 viscosity method consists of adding dissipative terms, with a viscosity coeffi-
 68 cient modulated by the entropy production which allows high-order accuracy
 69 when the solution is smooth. Thus, two questions arise: (i) how are the viscos-
 70 ity dissipative terms derived and (ii) how to numerically compute the entropy
 71 production. Answers to the first question can be found in [3] by Guermond et
 72 al., that details the proof leading to the derivation of the artificial dissipative
 73 terms (Eq. (2)) consistent with the entropy minimum principle theorem. The
 74 viscous regularization obtained is valid for any equation of state as long as the
 75 opposite of the physical entropy function, s , is convex with respect to the in-
 76 ternal energy e and the specific volume $1/\rho$. As for the entropy production, it
 77 is locally evaluated by computing the local entropy residual $D_e(\vec{x}, t)$ defined in
 78 Eq. (4), that is known to be peaked in shocks [17].

$$\begin{cases} \partial_t (\rho) + \vec{\nabla} \cdot (\rho \vec{u}) = \vec{\nabla} \cdot (\kappa \vec{\nabla} \rho) \\ \partial_t (\rho \vec{u}) + \vec{\nabla} \cdot (\rho \vec{u} \otimes \vec{u} + P \mathbf{I}) = \vec{\nabla} \cdot (\mu \rho \vec{\nabla}^s \vec{u} + \kappa \vec{u} \otimes \vec{\nabla} \rho) \\ \partial_t (\rho E) + \vec{\nabla} \cdot [\vec{u} (\rho E + P)] = \vec{\nabla} \cdot (\kappa \vec{\nabla} (\rho e) + \frac{1}{2} \|\vec{u}\|^2 \kappa \vec{\nabla} \rho + \rho \mu \vec{u} \vec{\nabla} \vec{u}) \\ P = P(\rho, e) \end{cases} \quad (2)$$

79 where κ and μ are local positive viscosity coefficients. $\vec{\nabla}^s \vec{u}$ denotes the sym-
 80 metric gradient operator that guarantees the method to be rotational invariant
 81 [3].

82 In the current version of the method, κ and μ are set equal, so that the above
 83 viscous regularization (Eq. (2)) is equivalent to the parabolic regularization
 84 [18] when considering the 1-D form of the equation. The current definition in-
 85 cludes a first-order viscosity coefficient referred to with the subscript *max*, and

a high-order viscosity coefficient referred to with the subscript e . The first-order viscosity coefficients μ_{max} and κ_{max} are proportional to the local largest eigenvalue $||\vec{u}|| + c$ and equivalent to an upwind-scheme (see Eq. (3)), when used, which is known to be over-dissipative and monotone [17]:

$$\mu_{max}(\vec{r}, t) = \kappa_{max}(\vec{r}, t) = \frac{h}{2} (||\vec{u}|| + c), \quad (3)$$

where h is defined as the ratio of the grid size to the polynomial order of the test functions used.

The second-order viscosity coefficients κ_e and μ_e are set proportional to the entropy production that is evaluated by computing the local entropy residual D_e . It also includes the interfacial jump of the entropy flux J that will allow to detect any discontinuities other than shocks:

$$\mu_e(\vec{r}, t) = \kappa_e(\vec{r}, t) = h^2 \frac{\max(|D_e(\vec{r}, t)|, J)}{||s - \bar{s}||_\infty} \text{ with } D_e(\vec{r}, t) = \partial_t s + \vec{u} \cdot \vec{\nabla} s \quad (4)$$

where $||\cdot||_\infty$ and $\bar{\cdot}$ denote the infinite norm operator and the average operator over the entire computational domain, respectively. The definition of the jump J is discretization-dependent and examples of definition can be found in [16] for DGFEM. The denominator $||s - \bar{s}||_\infty$ is used for dimensionality purposes and should not be of the same order as h , on penalty of loosing the high-order accuracy. Currently, there are no theoretical justification for choosing the denominator.

The definition of the viscosity coefficients μ and κ is function of the first- and second-order viscosity coefficients as follows:

$$\mu(\vec{r}, t) = \min(\mu_e(\vec{r}, t), \mu_{max}(\vec{r}, t)) \text{ and } \kappa(\vec{r}, t) = \min(\kappa_e(\vec{r}, t), \kappa_{max}(\vec{r}, t)). \quad (5)$$

This definition allows the following properties. In shock regions, the second-order viscosity coefficient experiences a peak because of entropy production, and thus, saturates to the first-order viscosity that is known to be over-dissipative and will smooth out oscillations. Anywhere else, the entropy production being small, the viscosity coefficients μ and κ are of order h^2 .

Using the above definition of the entropy-based viscosity method, high-order accuracy was demonstrated and excellent results were obtained with 1-D Sod shock tubes and various 2-D tests [1, 2, 16].

2.2. Issues in the Low-Mach Regime

In the Low-Mach Regime, the flow is known to be isentropic resulting in very little entropy production. Since the entropy viscosity method is directly based on the evaluation of the local entropy production, it will be interested to study how the entropy viscosity coefficients μ and κ scale in the low Mach regime. Mathematically, it means that the entropy residual D_e will be very small, so will be the denominator $||s - \bar{s}||_\infty$, thus making the ratio, used in the definition of the viscosity coefficients Eq. (4), undetermined. Therefore, the

current definition of the viscosity coefficients seems unadapted to subsonic flow and could lead to ill-scaled dissipative terms. A solution would be to recast the entropy residual as a function of other variables in order to have more freedom in the choice of the normalization parameter. With this approach, the viscosity coefficients are still defined proportional to the entropy residual that is a good indicator of the flow type (subsonic, transonic and supersonic flow). Plus, a different normalization parameter could be chosen, based on a low Mach asymptotic study so that the viscosity coefficients are well-scaled in the low Mach asymptotic limit (see Section 3).

2.3. The dissipative-terms for the multi-D Euler equations with variable area

One of the focus of this paper is to investigate the application of the entropy viscosity method to the multi-D Euler equations with variable area. The variable area version of the Euler equations is mostly used in 1-D and 2-D for obvious reasons, and differs from Eq. (1) by the momentum equation as shown in Eq. (6), that contains a non-conservative term proportional to the area gradient. For the purpose of this paper, the variable area is assumed to be a smooth function and only spatial dependent. An example can be found in [19] where a fluid flows through a 1-D convergent-divergent nozzle and reaches a steady-state solution.

$$\begin{cases} \partial_t (\rho A) + \vec{\nabla} \cdot (\rho \vec{u} A) = 0 \\ \partial_t (\rho \vec{u} A) + \vec{\nabla} \cdot [A (\rho \vec{u} \otimes \vec{u} + P \mathbf{I})] = P \vec{\nabla} A \\ \partial_t (\rho E) + \vec{\nabla} \cdot [\vec{u} (\rho E + P)] = 0 \end{cases} \quad (6)$$

The application of the entropy viscosity method to the above system of equations is expected to be straightforward since it degenerates to the Eq. (1) when assuming a constant area. Details of the derivations of the dissipative terms are available to the reader in Appendix B and are very similar to what was done in [3]. An entropy residual is derived without the dissipative terms. Then, the same entropy residual is re-derived after adding dissipative terms to each equation of the system given in Eq. (6), and the entropy minimum principle is used as a condition to obtain a definition for each of the dissipative terms. The final result including the dissipative terms is given in Eq. (7):

$$\begin{cases} \partial_t (\rho A) + \vec{\nabla} \cdot (\rho \vec{u} A) = \vec{\nabla} \cdot (A \kappa \vec{\nabla} \rho) \\ \partial_t (\rho \vec{u} A) + \vec{\nabla} \cdot [A (\rho \vec{u} \otimes \vec{u} + P \mathbf{I})] = P \vec{\nabla} A + \vec{\nabla} \cdot \left[A \left(\mu \rho \vec{\nabla}^s \vec{u} + \kappa \vec{u} \otimes \vec{\nabla} \rho \right) \right] \\ \partial_t (\rho E) + \vec{\nabla} \cdot [\vec{u} (\rho E + P)] = \vec{\nabla} \cdot \left[A \left(\kappa \vec{\nabla} (\rho e) + \frac{1}{2} \|\vec{u}\|^2 \kappa \vec{\nabla} \rho + \rho \mu \vec{u} \vec{\nabla} \vec{u} \right) \right] \end{cases} \quad (7)$$

The dissipative terms are very similar to the ones obtained for the multi-D Euler equations: each dissipative flux is multiplied by the variable area A in order to ensure conservation of the flux. When assuming a constant area, Eq. (2) is retrieved. The definition of the viscosity coefficients μ and κ is explained in Section 3.2.

153 3. All-speed Reformulation of the Entropy Viscosity Method

154 In this section, the entropy residual D_e is recast as a function of the pressure,
155 the density and the speed of sound. Then, a low Mach asymptotic study of the
156 multi-D Euler equations is performed in order to derive the correct normalization
157 parameter.

158 3.1. New Entropy Production Residual

159 The first step in defining a viscosity coefficient that behaves well in the low
160 mach limit is to recast the entropy residual in terms of the thermodynamic
161 variables as shown in Eq. (8):

$$D_e(\vec{r}, t) = \partial_t s + \vec{u} \cdot \vec{\nabla} s = \frac{s_e}{P_e} \left(\underbrace{\frac{dP}{dt} - c^2 \frac{d\rho}{dt}}_{\tilde{D}_e(\vec{r}, t)} \right), \quad (8)$$

162 where $\frac{d}{dt}$ denotes the material or total derivative, and P_e is the partial derivative
163 of pressure with respect to internal energy. The steps that lead to the new
164 formulation of the entropy residual D_e can be found in Appendix A.

165 The entropy residual D_e and \tilde{D}_e are proportional to each other and therefore
166 will experience the same variation when taking the absolute value. Thus, locally
167 evaluating \tilde{D}_e instead of D_e should allow us to measure the entropy production
168 point wise. This new expression given in Eq. (8) has multiple advantages:

- 169 • an analytical expression of the entropy function is not longer needed: the
170 entropy residual \tilde{D}_e is evaluated using the local values of the pressure, the
171 density and the speed of sound. Deriving an entropy function for some
172 complex equation of states can be difficult.
- 173 • with the proposed expression of the entropy residual function of pressure
174 and density, additional normalizations suitable for low Mach flows of the
175 entropy residual can be devised. Examples include the pressure itself,
176 or combination of the density, the speed of sound and the norm of the
177 velocity: ρc^2 , $\rho c ||\vec{u}||$ and $\rho ||\vec{u}||^2$.

178 The viscosity coefficients μ and κ are now defined proportional to the new
179 entropy residual \tilde{D}_e on the model of Eq. (4) as follows:

$$\mu(\vec{r}, t) = \kappa(\vec{r}, t) = h^2 \frac{\max(\tilde{D}_e, J)}{n(P)} \quad (9)$$

180 where $n(P)$ is a normalization parameter to determine and all other variables
181 were defined previously.

182 As mentioned earlier, the normalization parameter $n(P)$ must be of the same
183 units as the pressure for the viscosity coefficients to have the unit of a dy-
184 namic viscosity (m^2/s). Multiples options are available to us: P , ρc^2 , $\rho c ||\vec{u}||$

185 and $\rho||\vec{u}||^2$. The choice of the normalization parameter cannot be random if
 186 the definition of the viscosity coefficient is wanted to be well-scaled for a wide
 187 range of Mach numbers. For example, by choosing $n(P) = \rho||\vec{u}||^2$, the viscosity
 188 coefficient will become very large as the Mach number decreases which would
 189 be unnecessary since the equations will not develop any shock or discontinuity.
 190 Therefore, it is proposed to carry, in Section 3.2, a low-Mach asymptotic study
 191 of the multi-D Euler equations in order to determine the correct expression for
 192 the normalization parameter $n(P)$.

193 3.2. Low-Mach asymptotic study of the multi-D Euler equations

194 The asymptotic study requires the multi-D Euler equations to be non di-
 195 mensionalized: the objective is to make the Mach number appears and thus,
 196 use a polynomial expansion of the variables as a function of the Mach number
 197 in order to derive the leading, first- and second-order equations. Before detailing
 198 the steps of the asymptotic method, let us have a closer look at the system of
 199 equations under consideration. The initial system of equations is composed of
 200 the multi-D Euler equations. For stability purpose, artificial dissipative terms
 201 are added to each equation as explained in Section 2. The resulting system of
 202 equations is alike the multi-D Navier-Stokes equations in a sense that it con-
 203 tains second-order derivative terms. Thus, it would be interesting to look at the
 204 steps employed in the asymptotic study of the multi-D Navier-Stokes equations
 205 in order to understand how the dissipative terms are treated. Fortunately, this
 206 process is well-documented in the literature [10, 11, 12] for both multi-D Eu-
 207 ler equations and Navier-Stokes equations. The work presented here is mainly
 208 inspired of [20] that focuses on the asymptotic study in the low Mach regime
 209 of Navier-Stokes equations. During the derivation, the reader has to keep in
 210 mind that the objective of this section is to derive a normalization parameter
 211 for the definition of the viscosity coefficients so that the multi-D Euler equations
 212 degenerate to the incompressible system of equations, which implies that the
 213 dissipative terms are well-scaled. The main steps of the derivation are presented
 214 in the following of this section:

215 To express Eq. (2) in dimensionless variables, the following dimensional variables
 216 are introduced:

$$\begin{aligned} \rho &= \frac{\rho^*}{\rho_\infty}, P = \frac{P^*}{\rho_\infty c_\infty^2}, \mu = \frac{\mu^*}{\mu_\infty}, E = \frac{E^*}{c_\infty^2}, \mu = \frac{\mu^*}{\mu_\infty}, \\ \kappa &= \frac{\kappa^*}{\kappa_\infty}, x = \frac{x^*}{L_\infty}, t = \frac{t^*}{L_\infty/u_\infty}, u = \frac{u^*}{u_\infty} \end{aligned} \quad (10)$$

217 where the subscript ∞ and the upper script $*$ denote the far field or stagnation
 218 quantities and the dimensionless variables, respectively. The reference quantities
 219 are chosen such that the non dimensional flow quantities are of order one for
 220 any low reference-Mach number

$$M_\infty = \frac{u_\infty^*}{c_\infty^*} \quad (11)$$

221 where c_∞^* is a reference value for the speed of sound.
 222 Then, using the non dimensional quantities and the multi-D Euler equations
 223 from Eq. (2) , the following non dimensional form is obtained:

$$\left\{ \begin{array}{l} \partial_t \rho + \nabla \cdot (\rho \vec{u}) = \frac{1}{Re_\infty Pr_\infty} \nabla \cdot (\kappa \nabla \rho) \\ \partial_t (\rho \vec{u}) + \nabla \cdot (\rho \vec{u} \otimes \vec{u}) + \frac{1}{M_\infty^2} \nabla (P) = \frac{1}{Re_\infty} \nabla \cdot (\rho \mu \nabla \vec{u}) + \frac{1}{Re_\infty Pr_\infty} \nabla \cdot (\vec{u} \otimes \kappa \nabla \rho) \\ \partial_t (\rho E) + \nabla \cdot [\vec{u} (\rho E + P)] = \frac{1}{Re_\infty Pr_\infty} \nabla \cdot (\kappa \nabla (\rho e)) + \frac{M_\infty^2}{Re_\infty} \nabla \cdot (\vec{u} \rho \mu \nabla \vec{u}) \\ + \frac{M_\infty^2}{2 Re_\infty Pr_\infty} \nabla \cdot (\kappa u^2 \nabla \rho) \\ P = (\gamma - 1) (\rho E + M_\infty^2 \rho u^2) \end{array} \right.$$

224 where the *numerical* Reynolds (Re_∞) and Prandtl (Pr_∞) numbers are defined
 225 as follows:

$$Re_\infty = \frac{u_\infty L_\infty}{\mu_\infty} \text{ and } Pr_\infty = \frac{\mu_\infty}{\kappa_\infty}. \quad (12)$$

226 Since it is chosen to have the same definition for both μ and κ the numerical
 227 Prandtl number is unconditionally equal to one: $Pr_\infty = 1$.
 228 Once the dimensionless equations are obtained, the next step consists of expand-
 229 ing each variable in term of the Mach number (example given in Eq. (13) for
 230 the pressure P) in order to derive the leading, first- and second-order equations.

$$P(\vec{r}, t) = P_0(\vec{r}, t) + P_1(\vec{r}, t) M_\infty + P_2(\vec{r}, t) M_\infty^2 + \dots \text{ with } M_\infty \rightarrow 0 \quad (13)$$

231 Before deriving the leading-order equation, a choice needs to be made on how
 232 the numerical Reynolds number scales. Multiple options are available to us and
 233 a few example are given: $Re_\infty = M_\infty$, or $Re_\infty = M_\infty^{-1}$ or $Re_\infty = 1$. Let us
 234 assume for academy purpose that the numerical Reynolds number scales as the
 235 inverse of the Mach number square: $Re_\infty = M_\infty^{-2}$. The best way to evaluate the
 236 impact of this choice on the equations, is to look at the momentum equation
 237 and try to derive the order M_∞^{-2} :

$$\vec{\nabla} P_0 = \vec{\nabla} \cdot (\rho_0 \mu_0 \vec{\nabla} \vec{u}_0 + \vec{u}_0 \otimes \vec{\nabla} \rho_0) \quad (14)$$

238 which is known to be ([12])

$$\vec{\nabla} P_0 = 0 \quad (15)$$

239 It is clear that Eq. (14) and Eq. (15) will not yield the same result. The same
 240 conclusion is drawn when deriving the order M_∞^{-1} of the momentum equation,
 241 making our initial assumption not suitable. From the above result, it is under-
 242 stood that the numerical Reynolds number has to scale as one so that it does
 243 not affect the orders M_∞^{-2} and M_∞^{-1} of the momentum equations: $Re_\infty = 1$.

244 Thus, with such assumption, Eq. (12) implies:

At order M_∞^{-2} :

$$\vec{\nabla} P_0 = 0$$

At order M_∞^{-1} :

$$\vec{\nabla} P_1 = 0$$

At leading-order:

$$\begin{aligned} \partial_t \rho_0 &+ \vec{\nabla} \cdot (\rho_0 \vec{u}_0) = \vec{\nabla} \cdot (\kappa_0 \vec{\nabla} \rho_0) \\ \partial_t (\rho_0 \vec{u}_0) &+ \vec{\nabla} \cdot (\rho_0 \vec{u}_0 \otimes \vec{u}_0) + \vec{\nabla} P_2 = \vec{\nabla} \cdot (\rho_0 \mu_0 \vec{\nabla} \vec{u}_0 + \vec{u}_0 \otimes \vec{\nabla} \rho_0) \\ \partial_t (\rho_0 E_0) &+ \vec{\nabla} \cdot [\vec{u}_0 (\rho_0 E_0 + P_0)] = \vec{\nabla} \cdot (\kappa_0 \vec{\nabla} (\rho_0 e_0)) \end{aligned}$$

245 Under this form, the dissipative terms only affect the leading-order equations
246 in the asymptotic limit.

247 It is now determined that the numerical Reynolds number Re_∞ has to scale as
248 one. Following Eq. (12), Re_∞ is a function of the μ_∞ , and thus n_P . It can be
249 shown using Eq. (10) and the definitions of \tilde{D} given in Eq. (8) that:

$$\mu_\infty = \frac{\rho_\infty c_\infty^2 u_\infty L}{n_{P,\infty}} \quad (16)$$

250 where $n_{P,\infty}$ is the far-field quantity for the normalization parameter n_P . Sub-
251 stituting Eq. (16) into Eq. (12) and remembering that the numerical Reynolds
252 number scales as one, it yields:

$$n_{P,\infty} = \rho_\infty c_\infty^2 \quad (17)$$

253 Eq. (17) tells us that in the asymptotic limit, the normalization parameter n_P
254 scales as $\rho_\infty c_\infty^2$ which leaves us with two options: either $n_P = \rho c^2$ or $n_P = P$.
255 The choice was made to use $n_P = \rho c^2$ in the asymptotic limit: it was found
256 to behave well and the pressure can become locally negative and null in some
257 particular case as shown in Section 5. This normalization parameter is only valid
258 in the asymptotic limit and the purpose of this paper is to define a viscosity
259 coefficient μ that is valid for a wide range of Mach numbers. Thus, it is proposed
260 to define the high-order viscosity coefficient μ_e as follows:

$$\mu_e = h^2 \frac{\max(\tilde{D}_e, J)}{(1 - f(M))\rho c^2 + f(M)\rho ||\vec{u}||^2} \quad (18)$$

261 where $f(M)$ is a function of the local Mach number M with the following prop-
262 erties:

$$\begin{cases} f(M) \rightarrow 0 \text{ as } M \rightarrow 0 \\ f(M) \rightarrow 1 \text{ as } M \geq 1 \end{cases} \quad (19)$$

263 The choice of the function $f(M)$ is not fixed and a few examples are available
264 in the literature. A simple definition is $f(M) = \min(M, 1)$ which meets the
265 conditions of Eq. (19). Another definition for $f(M)$ was proposed by [13].

266 All of the numerical results presented in Section 5 were obtained by using
 267 $f(M) = \min(M, 1)$ which is simple to implement. A convergence test for a
 268 subsonic flow over a 2-D cylinder will show that this definition of $f(M)$ yields
 269 the correct behavior in the asymptotic limit. The definition of the high-order
 270 viscosity coefficient $\mu_e(\vec{r}, t)$ should behave well for complex flow where a near
 271 incompressible regime coexists with a supersonic flow domain since $f(M)$ is
 272 function of the local Mach number.
 273 For clarity purpose, the full definition of the viscosity coefficient $\mu(\vec{r}, t)$ is re-
 274 called:

$$\left\{ \begin{array}{l} \mu(\vec{r}, t) = \max(\mu_{max}(\vec{r}, t), \mu_e(\vec{r}, t)) \\ \text{where } \mu_{max}(\vec{r}, t) = \frac{h}{2}(\|\vec{u}\| + c) \\ \text{and } \mu_e(\vec{r}, t) = h^2 \frac{\max(\bar{D}_e, J)}{(1-f(M))\rho c^2 + f(M)\rho\|\vec{u}\|^2} \\ \mu(\vec{r}, t) = \kappa(\vec{r}, t) \end{array} \right. \quad (20)$$

275 These viscosity coefficients are valid for both the multi-D Euler equations with
 276 variable and constant area and are employed with the dissipative terms detailed
 277 in Eq. (12). The reader will notice that, through the derivation, none assumption
 278 was made on the type of equation of state besides the convexity condition on
 279 the entropy function s . The remaining of this paper (Section 5) will focus on
 280 demonstrating that the definition of the viscosity coefficient given in Eq. (20) is
 281 indeed well-scaled in the asymptotic limit and that shocks are still well resolved.

282 4. Solution Techniques Spatial and Temporal Discretizations

283 In order to detail the partial and temporal discretization used for this study,
 284 the system of equations Eq. (7) is considered under the following form for sim-
 285 plicity:

$$\partial_t U + \vec{\nabla} \cdot F(U) = S \quad (21)$$

286 where U is the vector solution, F is a conservative vector flux and S is a vector
 287 source that can contain the non-conservative term $P\vec{\nabla}A$.

288 4.1. Spatial and Temporal Discretizations

289 The system of equation given in Eq. (21) is discretized using a continuous
 290 Galerkin finite element method and high-order temporal integrators provided
 291 by the MOOSE framework.

292 4.1.1. CFEM

293 In order to apply the continuous finite element method, Eq. (21) is multiplied
 294 by a smooth test function ϕ , integrated by part and each integral is split onto
 295 each finite element e of the discrete mesh Ω bounded by $\partial\Omega$, to obtain a weak
 296 solution:

$$\sum_e \int_e \partial_t U \phi - \sum_e \int_e F(U) \cdot \vec{\nabla} \phi + \int_{\partial\Omega} F(U) \vec{n} \phi - \sum_e \int_e S \phi = 0 \quad (22)$$

297 The integrals over the elements e are evaluated using quadrature-point rules.
 298 The Moose framework provides a wide range of test function and quadrature
 299 rules: trapezoidal and Gauss rules among others. Linear Lagrange polynomials
 300 will be used as test functions and should ensure second-order convergence for
 301 smooth functions. The order of convergence will be demonstrated.

302 4.1.2. Temporal integrator

303 The MOOSE framework offers both first- and second-order explicit and im-
 304 plicit temporal integrators. In all of the numerical examples presented in Sec-
 305 tion 5, the time-dependent term $\int_e \partial_t U \phi$ will be evaluated using the second-order
 306 temporal integrator BDF2. By considering three solutions, U^{n-1} , U^n and U^{n+1}
 307 at three different time t^{n-1} , t^n and t^{n+1} , respectively, it yields:

$$\begin{aligned} \int_e \partial_t U \phi &= \int_e (\omega_0 U^{n+1} + \omega_1 U^n + \omega_2 U^{n-1}) \phi & (23) \\ \text{with } \omega_0 &= \frac{2\Delta t^{n+1} + \Delta t^n}{\Delta t^{n+1} (\Delta t^{n+1} + \Delta t^n)}, \\ \omega_1 &= -\frac{\Delta t^{n+1} + \Delta t^n}{\Delta t^{n+1} \Delta t^n} \\ \text{and } \omega_2 &= \frac{\Delta t^{n+1}}{\Delta t^n (\Delta t^{n+1} + \Delta t^n)} \end{aligned}$$

308 where $\Delta t^n = t^n - t^{n-1}$ and $\Delta t^{n+1} = t^{n+1} - t^n$.

309 4.2. Boundary conditions

310 The boundary conditions will be treated by either using Dirichlet or Neu-
 311 mann conditions. The multi-D Euler equations are wave-dominated systems
 312 that require great care when dealing with boundary conditions. It is often rec-
 313 ommended to use the characteristic equations to compute the correct flux at the
 314 boundaries. Our implementation of the subsonic boundary conditions will fol-
 315 low the method described in [19] that was developed for Ideal Gas and Stiffened
 316 Gas equation of states. For each numerical solution presented in Section 5, the
 317 type of boundary conditions used will be specified and taken among the follow-
 318 ings: supersonic inlet, subsonic inlet (stagnation pressure boundary), supersonic
 319 outlet and subsonic inlet (static pressure boundary).

320 4.3. Solver

321 A Free-Jacobian-Newton-Krylov (FJNK) method is used to solve for the
 322 solution at each time step. The jacobian matrix of the discretized equations
 323 was derived by hand, hard coded and used as a preconditioner. This method
 324 requires the partial derivative of the pressure with respect to the conservative
 325 variables to be known. The contribution of the artificial dissipative terms to
 326 the jacobian matrix is simplified by assuming constant viscosity coefficients as
 327 shown in Eq. (24) for the dissipative terms of the continuity equation:

$$\frac{\partial}{\partial U_i} \left(\kappa \vec{\nabla} \rho \vec{\nabla} \phi \right) = \kappa \frac{\partial}{\partial U_i} (\rho) \vec{\nabla} \phi \quad (24)$$

where U_i denotes the set of conservative variables.

5. Numerical Results

This section is dedicated to presenting 1- and 2-D numerical results obtained by solving Eq. (7) with the entropy viscosity method. This section has two objectives: validate our new definition of the viscosity coefficients for the low Mach limit, and, make sure that the new definition can still resolve shocks.

The first set of 1-D simulations consist of liquid water and steam flowing in a convergent-divergent nozzle. This test is interesting for multiple reasons: a steady-state is reached (some stabilization methods are known to have difficulties to reach a steady-state ([4, 5])), it can be performed for liquid and gas phases, and, an analytical solution of the steady-state solution is available which allow for convergence study. The 1-D Leblanc shock tube test [21] (in a straight pipe) is also performed and consists of a flow developing shocks. A convergence study will be performed in order to demonstrate convergence of the numerical solution to the exact solution.

This section also included 2-D simulations from subsonic to supersonic flows. Subsonic flows of a gas over a 2-D cylinder and a hump [22] are simulated and results are shown for various far-field Mach numbers. Numerical results of a supersonic flow in a compression corner are provided to illustrate the capabilities of the new definition in the supersonic case. Convergence studies are performed when an analytical solution is available.

For each simulation, informations relative to the boundary conditions and the equation of state will be provided. All of the numerical solution presented in this section are run with the second-order temporal integrator *BDF2* and linear polynomials test functions. The integrals are numerically computed using a second-order Gauss quadrature rule. The Ideal Gas [23] or Stiffened Gas equation of state [24] are used and a generic formulation is recalled in Eq. (25).

$$P = (\gamma - 1)\rho(e - q) - \gamma P_\infty \quad (25)$$

where the parameters q and P_∞ are fluid dependent and will be specified in time. Eq. (25) degenerates to the Ideal Gas equation of state by setting q and P_∞ to zero. The Ideal and Stiffened Gas equation of states have a convex entropy s :

$$s = C_v \ln \left(\frac{P + P_\infty}{\rho^{\gamma-1}} \right)$$

5.1. Liquid water in a 1-D divergent-convergent nozzle

The simulation consists of liquid water flowing through a 1-D convergent-divergent nozzle with the following equation, $A(x) = 1 + 0.5 \cos(2\pi x/L)$, where $L = 1m$ is the length of the nozzle. At the inlet, the stagnation pressure and temperature are set to $P_0 = 1MPa$ and $T_0 = 453K$, respectively. At the outlet, only the static pressure is specified: $P_s = 0.5MPa$. Details about the theory related to the inlet and outlet boundary conditions can be found in [19].

Initially, the temperature is uniform and set equal to the stagnation temperature and the pressure linearly decreases from the stagnation pressure to the static one. Finally, the liquid is assumed at rest. The Stiffened Gas equation of state is used to model the liquid water with the parameters provided in Table 1.

Table 1: Stiffened Gas Equation of State parameters for liquid water.

γ	$C_v (J \cdot kg^{-1} \cdot K^{-1})$	$P_\infty (Pa)$	$q (J \cdot kg^{-1})$
2.35	1816	10^9	-1167.10^3

Because of the low pressure difference between the inlet and the outlet, and the large value of P_∞ , the flow remains subsonic and thus, should not display any shock. Enthalpy and entropy are conserved through the nozzle, and these conservation relations are used to determine the exact solution at steady-state [25]. Plots of the velocity, density and pressure are given at steady-state in Fig. 1a, Fig. 1b, Fig. 1c, respectively, along with the exact solution for comparison. The viscosity coefficients are also plotted in Fig. 1d. The mesh used is uniform and has 50 cells.

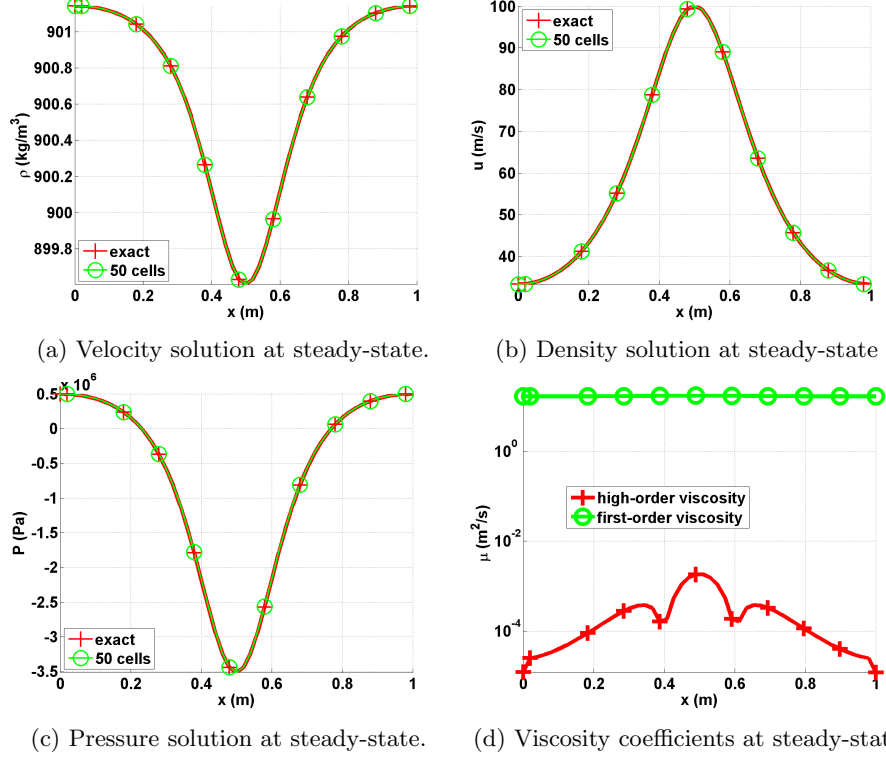


Figure 1: Steady-state solution for liquid phase in a 1-D convergent-divergent nozzle with an uniform mesh of 50 cells.

377 The numerical and exact solutions of the velocity, pressure and density given
 378 in Fig. 1 for a fairly coarse mesh (50 cells) perfectly overlap: it is noted that
 379 the numerical solution is symmetric with respect to the nozzle throat located
 380 in $x = 0.5m$. The second-order viscosity coefficient is very small compare to
 381 the first-order one as expected: (i) the numerical solution is smooth as shown
 382 in Fig. 1d and (ii) the flow is in a low Mach regime and thus isentropic . A
 383 convergence study was performed using the exact solution as a reference: the
 384 L1 and L2 norms of the error and the corresponding convergence rates are
 385 computed at steady-state on various uniform mesh from 4 to 256 cells. The
 386 results for linear polynomials Q_1 are reported in Table 2 and Table 3 for the
 387 primitive variables: density, velocity and pressure.

Table 2: L1 norm of the error for the liquid phase in a 1-D convergent-divergent nozzle at steady-state.

cells	density	rate	pressure	rate	velocity	rate
4	$2.8037 \cdot 10^{-1}$	—	$8.4705e \cdot 10^5$	—	7.2737	—
8	$1.3343 \cdot 10^{-1}$	1.0713	$4.7893e \cdot 10^5$	0.24227	6.1493	0.074683
16	$2.9373 \cdot 10^{-2}$	2.1835	$1.0613e \cdot 10^5$	2.3247	1.2275	2.4501
32	$5.1120 \cdot 10^{-3}$	2.5225	$1.8446 \cdot 10^4$	2.6959	$1.8943 \cdot 10^{-1}$	3.0966
64	$1.0558 \cdot 10^{-3}$	2.2755	$3.7938 \cdot 10^3$	2.3207	$3.7919 \cdot 10^{-2}$	2.3323
128	$2.3712 \cdot 10^{-4}$	2.1547	$8.4471 \cdot 10^2$	2.0624	$8.5517 \cdot 10^{-3}$	2.0473
256	$5.6058 \cdot 10^{-5}$	2.0806	$1.9839 \cdot 10^2$	2.0478	$2.0475 \cdot 10^{-3}$	1.9833
512	$1.3278 \cdot 10^{-5}$	2.0778	46.622	2.0478	$4.9516 \cdot 10^{-4}$	1.9669

Table 3: L2 norm of the error for the liquid phase in a 1-D convergent-divergent nozzle at steady-state.

cells	density	rate	pressure	rate	velocity	rate
4	$3.106397 \cdot 10^{-1}$	—	$5.254445 \cdot 10^5$	—	3.288543	—
8	$7.491623 \cdot 10^{-2}$	2.07	$1.636966 \cdot 10^5$	1.60	1.823880	0.90
16	$2.079858 \cdot 10^{-2}$	1.80	$4.627338 \cdot 10^4$	1.75	$4.990605 \cdot 10^{-1}$	1.83
32	$5.329627 \cdot 10^{-3}$	1.90	$1.180287 \cdot 10^4$	1.92	$1.261018 \cdot 10^{-1}$	1.93
64	$1.341583 \cdot 10^{-3}$	1.94	$2.967104 \cdot 10^3$	1.98	$3.160914 \cdot 10^{-2}$	1.99
128	$3.359766 \cdot 10^{-4}$	1.99	$7.428087 \cdot 10^2$	1.99	$7.907499 \cdot 10^{-3}$	1.99
256	$8.403859 \cdot 10^{-5}$	1.99	$1.857861 \cdot 10^2$	1.99	$1.977292 \cdot 10^{-3}$	1.99
512	$2.10075 \cdot 10^{-5}$	1.99	27.048	1.99	$4.9516 \cdot 10^{-4}$	1.99

388 It is observed that the convergence rate for the L1 and L2 norm of the error
389 is 2: the entropy viscosity method conserves the high-order accuracy when the
390 numerical solution is smooth, and the new definition of the entropy viscosity
391 coefficient seems to behave as expected in the low Mach limit.

392 5.2. Steam in a 1-D divergent-convergent nozzle

393 Instead of liquid water, we now simulate a flow of steam using the exact same
394 1-D geometry, initial conditions and boundary conditions as in Section 5.1. The
395 Stiffened gas equation of state is still used but with different parameters that are
396 given in Table 4: steam is a gas and compressible effects will become dominant.

Table 4: Stiffened Gas Equation of State parameters for steam.

γ	$C_v \text{ (} J \cdot kg^{-1} \cdot K^{-1} \text{)}$	$P_\infty \text{ (Pa)}$	$q \text{ (} J \cdot kg^{-1} \text{)}$
1.43	1040	0	$2030 \cdot 10^3$

397 The pressure difference applied between the inlet and outlet is large enough
 398 to make the steam accelerates through the nozzle and result in the formation of
 399 shock in the divergent part. The behavior is different from what is observed for
 400 the liquid water phase in Section 5.1 because of the liquid to gas density ratio
 401 that is of 1000. Even though a shock forms, an exact solution at steady-state
 402 is still available [25]. The objective of this section is to show that using the
 403 new definition of the viscosity coefficient in Eq. (20), the shock can be correctly
 404 resolved without spurious oscillation. The steady-state numerical solution is
 405 shown in Fig. 2 and was run with a mesh of 1600 cells.

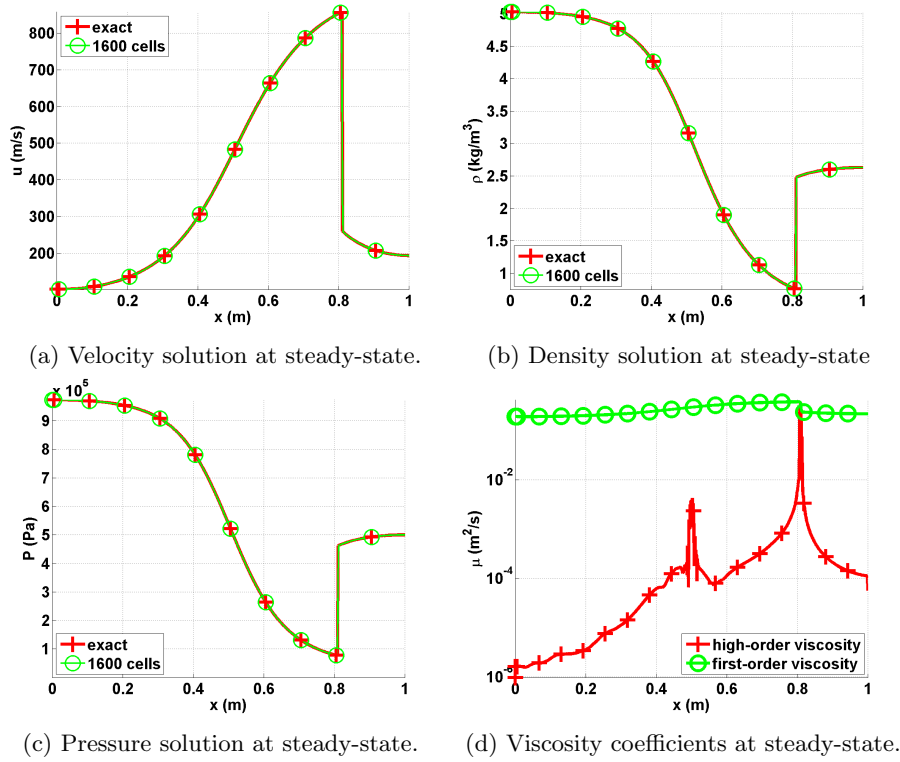


Figure 2: Steady-state solution for vapor phase in a 1-D convergent-divergent nozzle.

406 The steady-state solution of the density, velocity and pressure are given
 407 in Fig. 2a, Fig. 2b and Fig. 2c. The steady-solution displays a shock around
 408 $x = 0.8m$ and match the exact solution. In Fig. 2d, the first- and second-
 409 order viscosity coefficients are log plotted at steady-state: the second-order
 410 viscosity coefficient is peaked in the shock region around $x = 0.8m$ as expected,
 411 and saturate to the first-order viscosity coefficient. The profile also displays
 412 another peak at $x = 0.5m$ that corresponds to the position of the sonic point

for a 1-D convergent-divergent nozzle: this particular point is known to develop small instabilities that are detected when computing the jumps of the pressure and density gradients. Anywhere else, the second-order viscosity coefficient is small. In order to prove convergence of the numerical solution to the exact solution, a convergence study is performed. Because of the presence of a shock, second-order accuracy cannot be achieved. However, the convergence rate of a numerical solution containing a shock is known and expected to be of 1 and 1/2 when computing the L1 and L2 norms of the error, respectively (see Theorem 9.3 in [26]). Results are reported in Table 5 and Table 6 for the primitive variables: density, velocity and pressure.

Table 5: L1 norm of the error for the vapor phase in a 1-D convergent-divergent nozzle at steady-state.

cells	density	rate	pressure	rate	velocity	rate
5	$0.72562 \cdot 10^{-1}$	—	$1.5657 \cdot 10^5$	—	173.69	—
10	$0.4165 \cdot 10^{-1}$	0.80088	$9.6741 \cdot 10^4$	0.63425	120.69	0.52519
20	$0.20675 \cdot 10^{-1}$	1.0104	$4.9193 \cdot 10^4$	0.96971	72.149	0.74228
40	$0.093703 \cdot 10^{-1}$	1.1417	$2.0103 \cdot 10^4$	0.72728	34.716	1.0554
80	$0.047328 \cdot 10^{-1}$	0.9854	$1.0208 \cdot 10^4$	0.9777	16.082	1.1101
160	$0.023965 \cdot 10^{-2}$	0.9817	$5.1969 \cdot 10^3$	0.9739	7.9573	1.0150
320	$0.020768 \cdot 10^{-2}$	0.9886	$2.5116 \cdot 10^3$	1.0490	3.7812	1.0734
640	$0.0059715 \cdot 10^{-2}$	1.0160	$1.2754 \cdot 10^3$	0.9776	1.8353	1.0428

Table 6: L2 norm of the error for the vapor phase in a 1-D convergent-divergent nozzle at steady-state.

cells	density	rate	pressure	rate	velocity	rate
5	$9.7144 \cdot 10^{-1}$	—	$2.0215 \cdot 10^5$	—	236.94	—
10	$5.9718 \cdot 10^{-1}$	0.70195	$1.3024 \cdot 10^5$	0.63425	166.56	0.50854
20	$2.9503 \cdot 10^{-1}$	1.0173	$6.6503 \cdot 10^4$	0.96971	103.36	0.68831
40	$1.8193 \cdot 10^{-1}$	0.69747	$4.0171 \cdot 10^4$	0.72728	66.374	0.6390
80	$1.3366 \cdot 10^{-1}$	0.44485	$2.3163 \cdot 10^4$	0.43576	42.981	0.62692
160	$9.6638 \cdot 10^{-2}$	0.46790	$1.7263 \cdot 10^4$	0.42413	31.717	0.43844
320	$7.0896 \cdot 10^{-2}$	0.44688	$1.2763 \cdot 10^4$	0.43571	23.138	0.45499
640	$5.2191 \cdot 10^{-2}$	0.44190	$9.4217 \cdot 10^3$	0.43790	16.910	0.45238

The convergence rates for the L1 and L2 norms of the error are close to the theoretical values which prove convergence of the numerical solution to the exact solution.

It is also interesting to investigate the effect of the first-order viscosity onto the steady-state solution. In Fig. 3, the steady-state velocity profile is plotted when using the first- and second-order viscosity coefficients: the main difference

429 between the two numerical solution is in the resolution of the shock around
 430 $x = 0.8m$. The first-order viscosity coefficient is by definition more dissipative
 431 and will smooth out the solution. In the other hand, the high-order viscosity
 432 better resolves the shock and allow high-order accuracy away from the shock
 433 region. It is also noted that the numerical solution obtained with the first-order
 434 viscosity coefficient is satisfying: this is due to the nature of the solution that
 435 contains a standing shock, and thus, will force the shock to form even with large
 436 artificial dissipation.

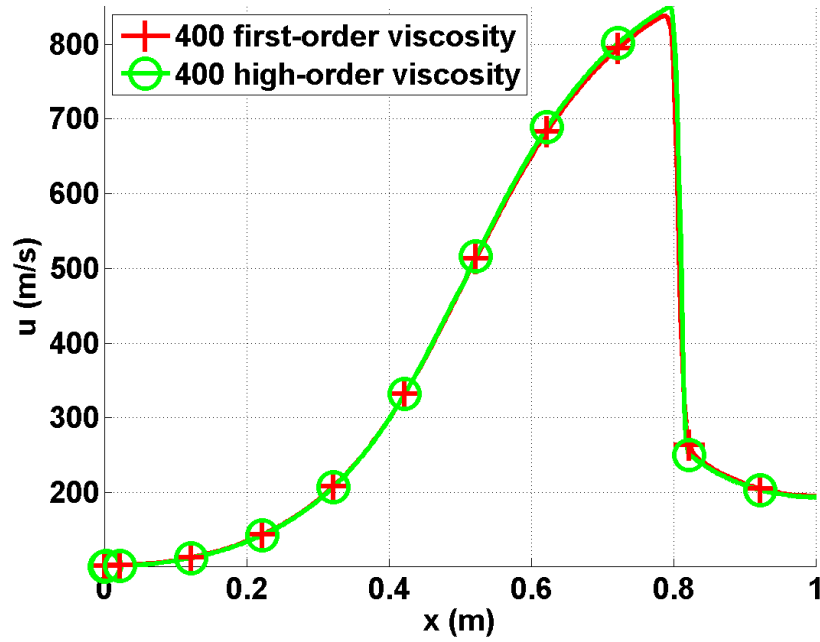


Figure 3: Velocity profile at steady-state with the first- and second-order viscosity for a mesh with 400 cells.

437 5.3. Leblanc shock tube

438 The 1-D Leblanc shock tube is a Riemann problem designed to test the
 439 robustness and the accuracy of the stabilization method. The initial conditions
 440 are given in Table 7. The ideal gas equation of state is used to compute the
 441 fluid pressure with the following heat capacity ratio $\gamma = 5/3$.

Table 7: Initial conditions for the 1-D Leblanc shock tube.

	ρ	u	e
left	1.	0.	0.1
right	10^{-3}	0.	10^{-7}

442 This test is computationally challenging because of the large left to right
 443 pressure ratio. The computational domain consists of a 1-D pipe of length
 444 $L = 9m$ with an interface located at $x = 2m$. At $t = 0.s$, the interface is
 445 removed, allowing the fluid to move. The numerical solution is run until $t = 4.s$
 446 and the density, momentum and total energy profiles are given in Fig. 4a, Fig. 4b
 447 and Fig. 4c, respectively, along with the exact solution. The viscosity coefficients
 448 are also plotted in Fig. 4d. These plots were run with three different uniform
 449 mesh of 800, 3200 and 6000 cells and a constant time step $\Delta t = 10^{-3}s$.

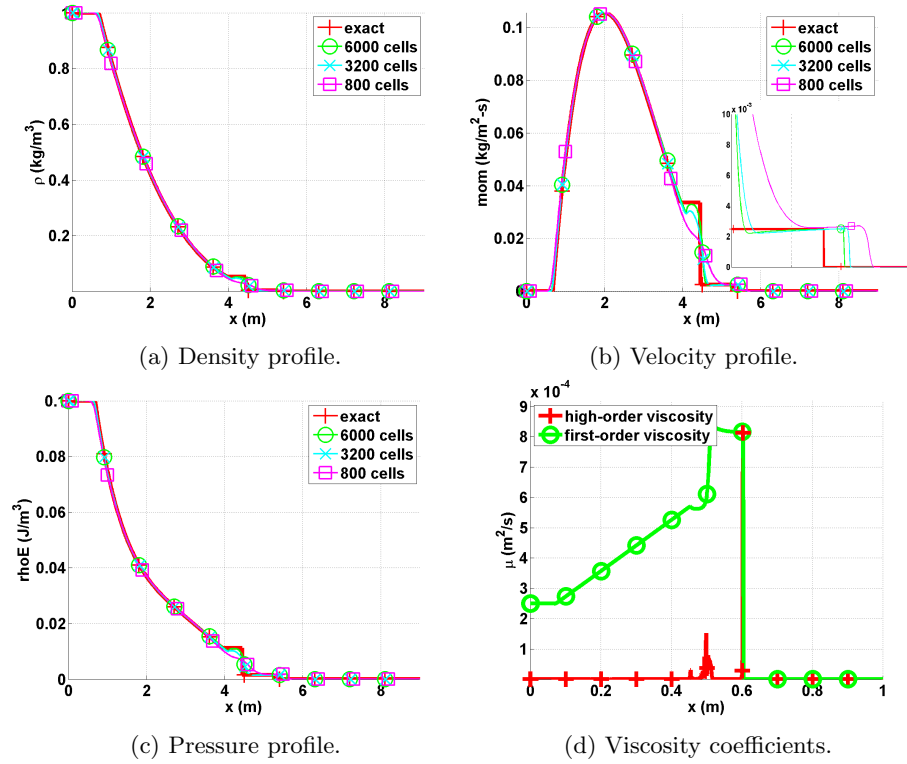


Figure 4: Numerical solution for the 1-D Leblanc shock tube at $t = 4.s$.

450 The density, momentum and total energy profiles given in Fig. 4 do not
 451 display any oscillations. In Fig. 4b, the shock region is zoomed in for better
 452 resolution: the shock is well resolved and do not show any oscillation. It is

453 also observed that the shock position of the numerical solution converges to the
 454 exact position when refining the mesh. The contact wave is shown in Fig. 4b at
 455 $x = 4.5m$. The second-order viscosity coefficient profile is shown in Fig. 4d and
 456 behaves as expected: it saturates to the first-order viscosity in the shock region
 457 and thus prevent oscillations from forming. In the contact wave at $x = 4.5m$, a
 458 smaller peak is observed that is due to the presence of the jumps in the definition
 459 of the second-order viscosity coefficient (Eq. (20)).
 460 Once again, a convergence study is performed in order to prove convergence of
 461 the numerical solution to the exact solution. As for the vapor phase in the 1-D
 462 nozzle (Section 5.2), the expected convergence rate for the L1 and L2 norms
 463 of the error are 1 and 1/2, respectively. The exact solution was obtained by
 464 running a 1-D Riemann solver and used as a reference solution to compute the
 465 L1 and L2-norms of the error that are reported in Table 8 and Table 9 for the
 466 conservative variables: density, momentum and total energy.

Table 8: L1 norm of the error for the 1-D Leblanc test at $t = 4.s$.

cells	density	rate	momentum	rate
100	$1.0354722 \cdot 10^{-2}$	—	$3.5471714 \cdot 10^{-3}$	—
200	$7.2680512 \cdot 10^{-3}$	0.51064841	$2.5933119 \cdot 10^{-3}$	0.45187331
400	$5.0825628 \cdot 10^{-3}$	0.51601245	$2.0668092 \cdot 10^{-3}$	0.32739054
800	$3.4025056 \cdot 10^{-3}$	0.57895861	$1.4793838 \cdot 10^{-3}$	0.48240884
1600	$2.1649953 \cdot 10^{-3}$	0.65223363	$9.7152832 \cdot 10^{-4}$	0.6066684
3200	$1.2465433 \cdot 10^{-3}$	0.79643094	$5.5937409 \cdot 10^{-4}$	0.79644263
6400	$6.4476928 \cdot 10^{-4}$	0.95107804	$3.0244198 \cdot 10^{-4}$	0.88715502
12800	$3.3950948 \cdot 10^{-4}$	0.92533116	$1.5958118 \cdot 10^{-4}$	0.9223679

cells	total energy	rate
100	0.0014033046	—
200	$9.8611746 \cdot 10^{-4}$	0.5089968
400	$7.7844421 \cdot 10^{-4}$	0.34116585
800	$5.5702549 \cdot 10^{-4}$	0.48285029
1600	$3.5720171 \cdot 10^{-4}$	0.64100438
3200	$2.0491799 \cdot 10^{-4}$	0.80169235
6400	$1.0914891 \cdot 10^{-4}$	0.90874889
12800	$5.7909794 \cdot 10^{-5}$	0.91441847

Table 9: L2 norm of the error for the 1-D Leblanc test at $t = 4.s$.

cells	density	rate	momentum	rate
100	$5.7187851 \cdot 10^{-3}$	—	$1.7767236 \cdot 10^{-3}$	—
200	$3.8995238 \cdot 10^{-3}$	0.55241073	$1.4913161 \cdot 10^{-3}$	0.25263314
400	$2.8103526 \cdot 10^{-3}$	0.4725468	$1.3305301 \cdot 10^{-3}$	0.164585
800	$2.1081933 \cdot 10^{-3}$	0.41474398	$1.1398931 \cdot 10^{-3}$	0.22310254
1600	$1.5731052 \cdot 10^{-3}$	0.42239201	$9.0394227 \cdot 10^{-4}$	0.33459602
3200	$1.0610667 \cdot 10^{-3}$	0.56809979	$6.2735595 \cdot 10^{-4}$	0.52694639
6400	$7.3309974 \cdot 10^{-4}$	0.53343397	$4.4545754 \cdot 10^{-4}$	0.49399631
12800	$5.1020991 \cdot 10^{-4}$	0.52291857	$3.1266758 \cdot 10^{-4}$	0.5106583

cells	total energy	rate
100	$7.6112265 \cdot 10^{-4}$	—
200	$5.5497308 \cdot 10^{-4}$	0.45571115
400	$4.6063172 \cdot 10^{-4}$	0.26880405
800	$3.7798953 \cdot 10^{-4}$	0.28526749
1600	$2.9584646 \cdot 10^{-4}$	0.35349763
3200	$2.054455 \cdot 10^{-4}$	0.52609289
6400	$1.4670834 \cdot 10^{-4}$	0.48580482
12800	$1.0299897 \cdot 10^{-5}$	0.51032105

The convergence rates are close to the expected values which prove convergence of the numerical solution to the exact solution.

5.4. Subsonic flow over a 2-D cylinder

The flow of a fluid over a 2-D cylinder is a typical benchmark case to test the behavior of a numerical method in the low Mach regime. For this test, an analytical solution is available in the incompressible limit or low Mach limit (REFS) and often referred to as potential flow. The main features of the potential flow are the following:

- The solution is symmetric: the iso-mach number lines are used to assess the symmetry of the numerical solution.
- The velocity at the top of the cylinder is twice the incoming velocity set at the inlet.
- The pressure fluctuations are proportional to the inlet Mach number square, as follows:

$$\tilde{P} = \frac{\max(P) - \min(P)}{\max(P)} \propto M_{\infty}^2$$

where \tilde{P} and M_{∞} are the pressure fluctuations and the inlet Mach number, respectively.

483 The computational domain consists of a 1×1 square with a circular hole of radius
 484 0.05 in its middle. At the inlet, a subsonic stagnation boundary condition is
 485 used: the stagnation pressure and temperature are computed using the following
 486 relations, valid for the Stiffened and Ideal gas equation of states:

$$\begin{cases} P_0 = P \left(1 + \frac{\gamma-1}{2} M^2\right)^{\frac{\gamma}{\gamma-1}} \\ T_0 = T \left(1 + \frac{\gamma-1}{2} M^2\right) \end{cases} \quad (26)$$

487 The static pressure $P_s = 101325 \text{ Pa}$ is set at the subsonic outlet and a static
 488 pressure boundary type is used. The implementation of the pressure boundary
 489 conditions is done on the model of [19]. A solid wall boundary condition is set for
 490 the top and bottom walls of the computational domain: the normal velocity is
 491 zero since no mass can penetrate the solid body. The mesh is made of triangular
 492 cells.

493 The steady-state for Mach numbers ranging from $M_\infty = 10^{-3}$ to $M_\infty = 10^{-7}$
 494 is shown in Fig. 5. The iso-Mach lines are drawn with 50 intervals ranging from
 495 10^{-8} to $2M_\infty$, and allow to assess the symmetry of the numerical solution.

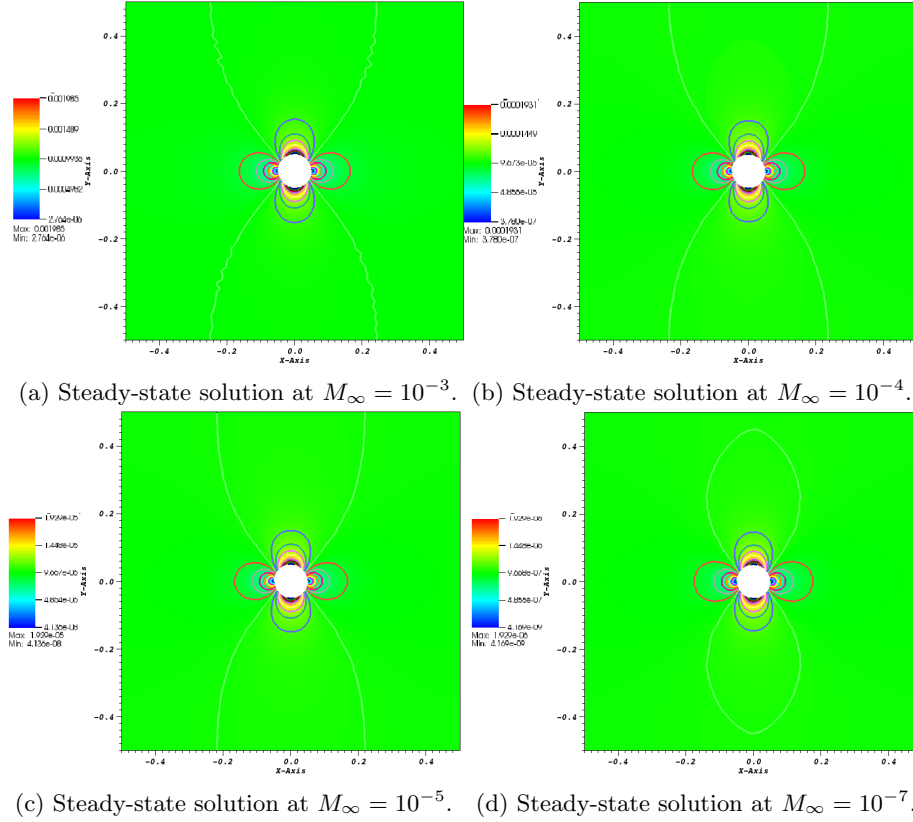


Figure 5: Steady-state solution for a subsonic flow over a 2-D cylinder.

496 In Table 10, the velocity at the top of the cylinder and at the inlet are given
 497 for the different values of the Mach number presented in Fig. 5. The ratio of
 498 the inlet velocity to the velocity at the top of cylinder is also computed and is
 499 very close to 2 as expected.

Table 10: Velocity ratio for different Mach numbers.

Mach number	inlet velocity	velocity at the top of the cylinder	ratio
10^{-3}	$2.348 \cdot 10^{-3}$	$1.176 \cdot 10^{-3}$	1.99
10^{-4}	$2.285 \cdot 10^{-4}$	$1.145 \cdot 10^{-4}$	1.99
10^{-5}	$2.283 \cdot 10^{-5}$	$1.144 \cdot 10^{-5}$	1.99
10^{-6}	$2.283 \cdot 10^{-6}$	$1.144 \cdot 10^{-6}$	1.99
10^{-7}	$2.283 \cdot 10^{-7}$	$1.144 \cdot 10^{-7}$	1.99

500 In Fig. 6, the pressure and velocity fluctuations are plotted (log-log plot) as
 501 a function of the far field Mach number. The pressure and velocity fluctuations
 502 are expected to be function of the Mach number square and the Mach number,
 503 respectively. For reference purpose, the function $f(M) = M^2$ and $f(M) = M$
 504 are plotted. The objective of Fig. 6 is to show that the new definition of the
 505 viscosity coefficients lead the correct convergence order in the low Mach limit.

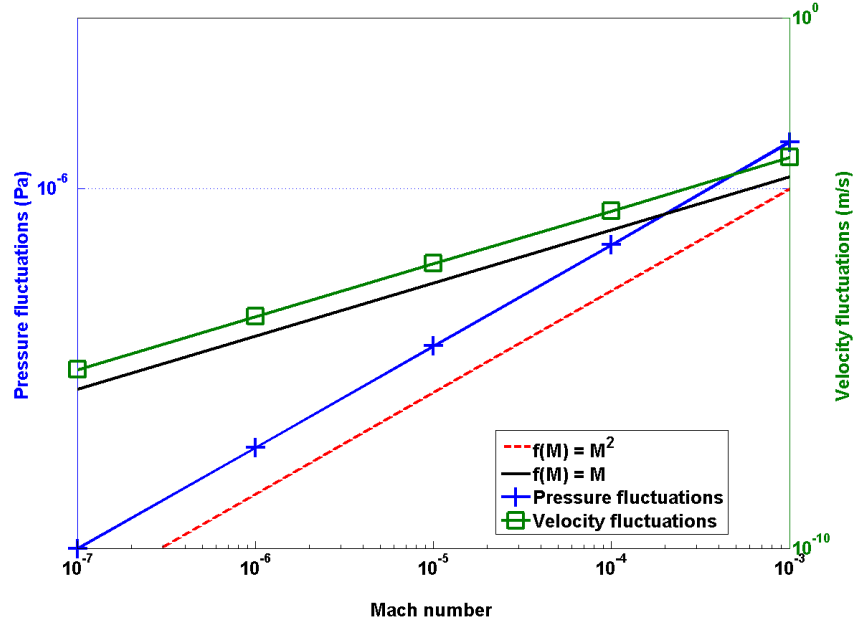


Figure 6: Log-log plot of the pressure and velocity fluctuations as a function of the far field Mach number.

5.5. Subsonic flow over a 2-D hump

This is a another example of an internal flow configuration. It consist of a channel of height $L = 1\text{ m}$ and length $3L$, with a circular bump of length L and thickness $0.1L$. The bump is located on the bottom wall at a distance L from the inlet. The system is initialized with an uniform pressure $P = 101325\text{ Pa}$ and temperature $T = 300\text{ K}$. The initial velocity is computed from the Mach number, M_∞ , the pressure, the temperature and the Ideal Gas equation of state with the heat capacity $C_v = 717\text{ J/kg} - \text{K}$ and the heat capacity ratio $\gamma = 1.4$. At the inlet, a subsonic stagnation boundary condition is used and the stagnation pressure and temperature are computed using Eq. (26). The static pressure $P_s = 101325\text{ Pa}$ is set at the subsonic outlet. An uniform grid is used to get the numerical solution until steady-state is reached. The results are shown in Fig. 7a, Fig. 7b, Fig. 7c and Fig. 7d for the inlet Mach numbers $M_\infty = 0.7$, $M_\infty = 0.01$, $M_\infty = 10^{-4}$ and $M_\infty = 10^{-7}$, respectively. It is expected that, within the low Mach number range, the solution does not depend on the Mach number and is identical to the solution obtained with an incompressible flow code. On the other hand, for a flow at $M = 0.7$, the compressible effects become more important and shock can form.

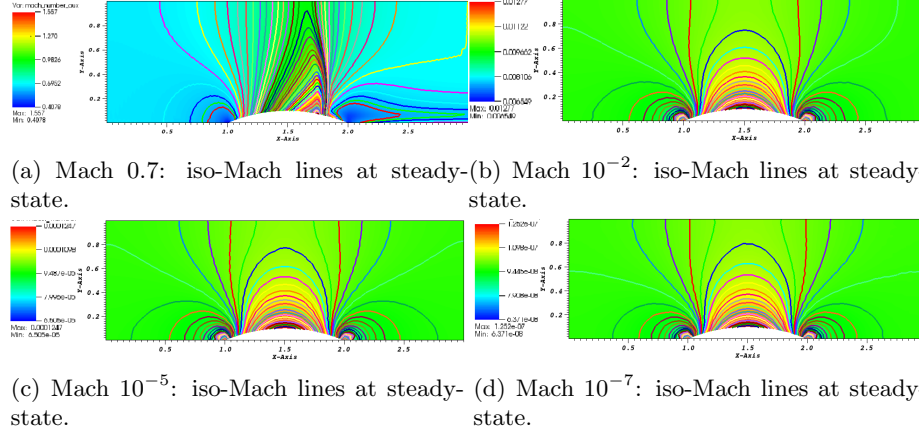


Figure 7: Steady-state solution for a 2-D flow over a circular bump.

The results showed in Fig. 7b, Fig. 7c and Fig. 7d correspond to the low Mach regime. The iso-Mach lines are drawn ranging from the minimum and the maximum of each legend with 50 intervals. The steady-state solution is symmetric and does not depend on the value of the inlet Mach number as expected. In Fig. 7a, the steady-state numerical solution develops a shock: the compressibility effect are no longer negligible. The iso-Mach lines are also plotted with 50 intervals and ranging from 0.4 to 1.6. The shock is well resolved and does not display any instability or spurious oscillation. The results presented in Fig. 7 were obtained with the new definition of the viscosity coefficient (see Eq. (20)), and, illustrate the capabilities of the entropy-

viscosity method to adapt to the type of flow (subsonic and transonic flows) without using any tuning parameters, but by just evaluating the entropy residual that is an indicator of the entropy production.

5.6. Supersonic flow in a compression corner

This is an example of a supersonic flow over a wedge of angle 15° where an oblique shock is generated at steady-state. The Mach number upstream of the shock is fixed to $M = 2.5$. The initial conditions are uniform: the pressure and temperature are set to $P = 101325 \text{ Pa}$ and $T = 300 \text{ K}$, respectively. The initial velocity is computed from the upstream Mach number and using the Ideal Gas equation of state with the same parameters as in Section 5.5. The code is run until steady-state. An analytical solution for this supersonic flow is available and give the downstream to upstream pressure, entropy and Mach number ratios [14]. The analytical and numerical ratios are given in see in Table 11, and are very close.

Table 11: Analytical solution for the supersonic flow on an edge eat 15° at $M = 2.5$.

	analytical downstream to upstream ratio	numerical downstream to upstream ratio
Pressure	2.47	2.467
Mach number	0.74	0.741
Entropy	1.03	1.026

The inlet is supersonic and therefore, the pressure, temperature and velocity are specified using Dirichlet boundary conditions. The outlet is also supersonic and none of the characteristics enter the domain through this boundary: the values will be computed by the implicit solver.

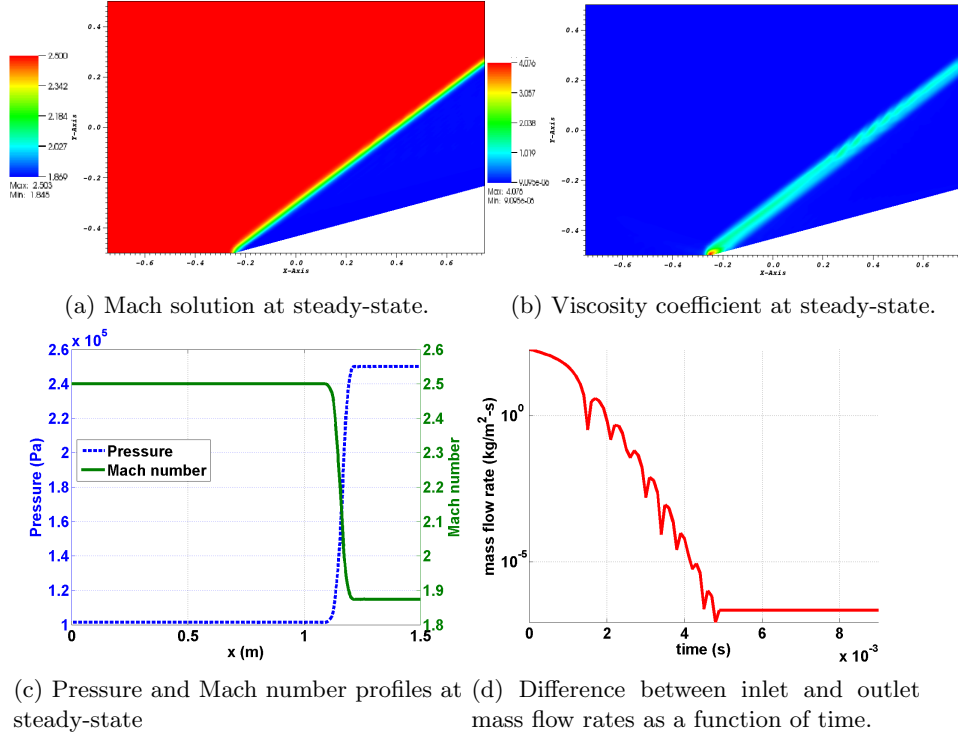


Figure 8: Steady-state solution for a flow in a 2-D compression corner.

552 The steady-state numerical solution is given in Fig. 8: the Mach number,
 553 the viscosity coefficients are plotted in Fig. 8a and Fig. 8b, respectively. The
 554 steady-state solution is formed of two regions of constant states, separated by
 555 the oblique shock. In Fig. 8b, the viscosity coefficient is large in the shock,
 556 small anywhere else, and thus, behaves as expected. At the corner of the edge
 557 at $x = -0.25$ m, the viscosity coefficient is peaked because of the treatment
 558 of the wall boundary condition: at this particular node, the normal is not well
 559 defined and can cause numerical errors. The 1-D plots of the pressure and the
 560 mach number at $y = 0$, are also given in Fig. 8c: the shock does not show any
 561 spurious oscillations and is well resolved. Finally, the difference between the
 562 inlet and outlet mass flow rates is plotted in Fig. 8d and show that the steady-
 563 state is reached.
 564 Overall, the numerical solution does not show any oscillations, match the ana-
 565 lytical solution, and the shock is well resolved.

566 6. Conclusions

567 A new version of the entropy viscosity method valid for a wide range of
 568 Mach number and applied to the multi-D Euler equations with variable area
 569 was derived and presented. The definition of the viscosity coefficient is now

570 consistent with the low Mach asymptotic limit, does not require an analytical
 571 expression of the entropy function, and thus, could be used with any equation
 572 of state having a convex entropy. Tests were performed with the Ideal and
 573 Stiffened Gas equation of states. In 1-D, convergence of the numerical solu-
 574 tion (either smooth or with shocks) to the exact solution was demonstrated by
 575 computing the convergence rates of the L1 and L2 norms of the error for flows
 576 in convergence-divergent nozzle and a straight pipe. 2-D simulations were also
 577 performed for both subsonic and supersonic flows, and various geometries: the
 578 entropy viscosity method behaves well for a wide range of Mach number. The
 579 numerical results obtained for a flow over a circular bump (subsonic and tran-
 580 sonic flows) illustrates the capabilities of the method to adapt to the flow type.
 581 As future work, the entropy viscosity method will be extended to the 1-D seven
 582 equations model [19]. This two-phase flow system of equations is a good can-
 583 didate for two reasons: it is unconditionally hyperbolic and degenerates to the
 584 multi-D Euler equations when one phase disappears.

585 Acknowledgments

586 The authors would like to thank Bojan Popov and Jean Luc Guermond for
 587 the many fruitful discussions.

588 References

- 589 [1] J. L. Guermond, R. Pasquetti, Entropy viscosity method for nonlinear con-
 590 servation laws, *Journal of Comput. Phys* 230 (2011) 4248–4267.
- 591 [2] J. L. Guermond, R. Pasquetti, Entropy viscosity method for high-order ap-
 592 proximations of conservation laws, *Lecture Notes in Computational Science*
 593 *and Engineering* 76 (2011) 411–418.
- 594 [3] J. L. Guermond, B. Popov, Viscous regularization of the euler equations
 595 and entropy principles, under review.
- 596 [4] B. Cockburn, C. Johnson, C. Shu, E. Tadmor, Advanced numerical approx-
 597 imation of nonlinear hyperbolic equations, *Lecture Notes in Mathematics*
 598 1697.
- 599 [5] B. Cockburn, G. Karniadakis, C. Shu, Discontinuous galerkin methods:
 600 theory, computation and applications, *Lecture Notes in Computer Science*
 601 *and Engineering* 11.
- 602 [6] R. Lohner, *Applied CFD Techniques: an Introduction based on Finite*
 603 *Element Methods*, 2nd Edition Wiley, 2003.
- 604 [7] A. Lapidus, A detached shock calculation by second order finite differences,
 605 *J. Comput. Phys.* 2 (1967) 154–177.

- 606 [8] R. Lohner, K. Morgan, J. Peraire, A simple extension to multidimensional
607 problems of the artificial viscosity due to lapidus, *Commun. Numer. Meth-*
608 *ods Eng.* 1(14) (1985) 141–147.
- 609 [9] J. Donea, A. Huerta, *Finite Element Methods for Flow Problems*, Oxford
610 University Press, 2003.
- 611 [10] H. Guillard, C. Viozat, On the behavior of upwind schemes in the low mach
612 number limit, *Computers & Fluids* 28 (1999) 63–86.
- 613 [11] E. Turkel, Preconditioned techniques in computational fluid dynamics,
614 *Annu. Rev. Fluid Mech.* 31 (1999) 385–416.
- 615 [12] J. S. W. D. L. Darmofal, J. Peraire, The solution of the compressible euler
616 equations at low mach numbers using a stabilized finite element algorithm,
617 *Comput. Methods Appl. Mech. Engrg.* 190 (2001) 5719–5737.
- 618 [13] X.-S. Li, C.-W. Gu, An all-speed roe-type scheme and its asymptotic anal-
619 ysis of low mach number behavior, *Journal of Computational Physics* 227
620 (2008) 5144–5159.
- 621 [14] J. D. Anderson, Modern compressible flow, in: *Guide for Verification and*
622 *Validation in Computational Solid Mechanic.*, New York, 1982, pp. 10–
623 2006.
- 624 [15] J. L. Guermond, R. Pasquetti, Entropy-based nonlinear viscosity for four-
625 rier approximations of conservation laws, in: *C.R. Math. Acad. Sci.*, Vol.
626 326, Paris, 2008, pp. 801–806.
- 627 [16] V. Zingan, J. L. Guermond, J. Morel, B. Popov, Implementation of the
628 entropy viscosity method with the discontinuous galerkin method, *Journal*
629 *of Comput. Phys* 253 (2013) 479–490.
- 630 [17] E. F. Toro, *Riemann Solvers and numerical methods for fluid dynamics*,
631 *2nd Edition*, Springer, 1999.
- 632 [18] B. Perthane, C. W. Shu, On positivity preserving finite volume schemes for
633 euler equations, *Numer. Math.* 73 (1996) 119–130.
- 634 [19] R. Berry, R. Saurel, O. LeMetayer, The discrete equation method (dem)
635 for fully compressible, two-phase flows in ducts of spatially varying cross-
636 section, *Nuclear Engineering and Design* 240 (2010) 3797–3818.
- 637 [20] B. Muller, Low-mach number asymptotes of the navier-stokes equations,
638 *Journal of Engineering Mathematics* 34 (1998) 97109.
- 639 [21] R. Loubere, Validation test case suite for compressible hydrodynamics com-
640 putation, Theoretical Division T-7 Los Alamos National Laboratory.

- 641 [22] D. L. Darmofal, K. Siu, A robust multigrid algorithm for the euler equations
 642 with local preconditioning and semi-coarsening, *Journal of Computational*
 643 *Physics* 151 (1999) 728756.
- 644 [23] P. Perrot, *A to Z of Thermodynamics*, Oxford University Press, 1998.
- 645 [24] O. LeMetayer, J. Massoni, R. Saurel, Elaborating equation of state for a
 646 liquid and its vapor for two-phase flow models, *International Journal of*
 647 *Thermal Science* 43 (2004) 265–276.
- 648 [25] S. LeMartelot, B. Nkonga, R. Saurel, Liquid and liquid-gas flows at all
 649 speeds: Reference solutions and numerical schemes., *Rsearch report* 7935.
- 650 [26] R. A. DeVore, G. G. Lorentz, *Constructive Approximation*, Springer-
 651 *Verlag*, 1991.

652 **A. Derivation of the entropy residual as a function of the density, the**
653 **pressure and the speed of sound:**

654 The entropy residual is often expressed as a function of the entropy $s(\vec{r}, t)$
655 as follows:

$$D_e(\vec{r}, t) = \partial_t s(\vec{r}, t) + \vec{u} \cdot \vec{\nabla} \cdot s(\vec{r}, t)$$

656 where all variables were defined previously. This form of the entropy residual is
657 not suitable for the low-Mach limit as explained in Section 2.1. It can be shown
658 that the entropy residual $D_e(\vec{r}, t)$ can be recast as a function of the primitive
659 variables (pressure, velocity and density) and the speed of sound. This is the
660 objective of this appendix.

661 The first step is to use the chain rule, remembering that the entropy is assumed
662 function of the internal energy e and the density ρ :

$$D_e(\vec{r}, t) = s_e \frac{de}{dt} + s_\rho \frac{d\rho}{dt}$$

663 where s_x denotes the partial derivative of s with respect to the variable x . The
664 short-notation $\frac{d}{dt}$ is used for the total or material derivative. We no need to
665 make the pressure appear: this can be achieved by noticing that the internal
666 energy is a function of the pressure and the density based on the definition of
667 the equation of state. Once again, by using the chain rule, it yields:

$$\begin{aligned} D_e(\vec{r}, t) &= s_e e_P \frac{dP}{dt} + (s_e e_\rho + s_\rho) \frac{d\rho}{dt} \\ &= s_e e_P \left(\frac{dP}{dt} + \frac{1}{s_e e_P} (s_e e_\rho + s_\rho) \frac{d\rho}{dt} \right) \\ &= s_e e_P \left(\frac{dP}{dt} + \left(\frac{e_\rho}{e_P} + \frac{s_\rho}{s_e e_P} \right) \frac{d\rho}{dt} \right) \end{aligned}$$

668 We are now close to the final result (see Eq. (8)). It remains to prove that the
669 term multiplying the material derivative of the density is equal to the speed
670 of sound square. The speed of sound is often defined as the partial derivative
671 of the pressure with respect to the density at constant entropy, which can be
672 recast as a function of the entropy as follows (see Appendix A.2 of [3]):

$$c^2 = \left(\frac{\partial P}{\partial \rho} \right)_s = P_\rho - \frac{s_\rho}{s_e} P_e = -\frac{e_\rho}{e_P} - \frac{s_\rho}{s_e e_P}$$

673 using the following relations (see Appendix A.1 of [3]):

$$P_e = \frac{1}{e_P} \text{ and } P_\rho = \frac{e_\rho}{e_P}$$

674 Then, the result follows.

675 **B. Derivation of the dissipative terms for the multi-D Euler equations**
676 **with variable area using the entropy minimum principle:**

677 The multi-D Euler equations with variable area are recalled here:

$$\begin{cases} \partial_t (\rho A) + \vec{\nabla} \cdot (\rho \vec{u} A) = 0 \\ \partial_t (\rho \vec{u} A) + \vec{\nabla} \cdot [A (\rho \vec{u} \otimes \vec{u} + P \mathbf{I})] = P \vec{\nabla} A \\ \partial_t (\rho E) + \vec{\nabla} \cdot [\vec{u} (\rho E + P)] = 0 \end{cases}$$

678 Assuming the existence of an entropy s function of the density ρ and the internal
679 energy e , the above system of equations admits the following entropy residual
680 [17]:

$$A \rho \left(\partial_t s + \vec{u} \cdot \vec{\nabla} \cdot s \right) \geq 0$$

681 when assuming $P s_e + \rho^2 s_\rho = 0$. An entropy function s verifying this equation
682 is also a solution of the second thermodynamic law for a reversible system,
683 $T ds = de - \frac{P}{\rho^2} d\rho$, which implies $s_e = T^{-1} \geq 0$.

684 In order to apply the entropy viscosity method, dissipative terms are added to
685 each equation. Then, the entropy residual is derived again: extra terms due to
686 the dissipative terms will appear in the left-hand side. In order to prove the
687 minimum entropy principle, these extra terms are either recast as conservative
688 term, or shown to be positive.

689 The multi-D Euler equations with variable area with dissipative terms, yield:

$$\begin{cases} \partial_t (\rho A) + \vec{\nabla} \cdot (\rho \vec{u} A) = \vec{\nabla} \cdot f \\ \partial_t (\rho \vec{u} A) + \vec{\nabla} \cdot [A (\rho \vec{u} \otimes \vec{u} + P \mathbf{I})] = P \vec{\nabla} A + \vec{\nabla} \cdot g \\ \partial_t (\rho E) + \vec{\nabla} \cdot [\vec{u} (\rho E + P)] = \vec{\nabla} \cdot h \end{cases} \quad (27)$$

690 where f , g and h are the dissipative terms to derive. Starting from the modified
691 system of equations given in Eq. (27), the entropy residual is derived again:

$$\begin{aligned} A \rho \left(\partial_t s + \vec{u} \cdot \vec{\nabla} \cdot s \right) &= s_e \left[\vec{\nabla} \cdot h + g \vec{\nabla} u + \left(\frac{u^2}{2} - e \right) \vec{\nabla} \cdot f \right] \\ &+ \rho s_\rho \vec{\nabla} \cdot f \end{aligned} \quad (28)$$

692 The next step consists of choosing a definition for each of the dissipative terms
693 so that the left hand-side is proven positive. The right hand-side of Eq. (28)
694 can be simplified using the following relations, $g = A \mu \vec{\nabla}^s \vec{u} + \vec{u} \otimes f$ and $h =$
695 $\tilde{h} + \vec{u} \cdot g - 0.5 ||\vec{u}||^2 f$, which yields:

$$A \rho \left(\partial_t s + \vec{u} \cdot \vec{\nabla} \cdot s \right) = s_e \left[\vec{\nabla} \cdot \tilde{h} - e \vec{\nabla} \cdot f \right] + \rho s_\rho \vec{\nabla} \cdot f + A s_e \mu \vec{\nabla}^s \vec{u} \cdot \vec{\nabla} \vec{u}$$

696 The right hand-side is now integrated by part:

$$\begin{aligned} A \rho \left(\partial_t s + \vec{u} \cdot \vec{\nabla} \cdot s \right) &= \vec{\nabla} \cdot \left[s_e \tilde{h} - s_e e f + \rho s_\rho f \right] - \\ &\vec{\nabla} \cdot \tilde{h} \vec{\nabla} s_e - f \vec{\nabla} (e s_e) - f \vec{\nabla} (\rho s_\rho) + A s_e \mu \vec{\nabla}^s \vec{u} \cdot \vec{\nabla} \vec{u} \end{aligned}$$

where $\vec{\nabla}^s$ is the symmetric gradient. The term $As_e\mu\vec{\nabla}\vec{u}^s\vec{\nabla}\vec{u}$ is positive and thus, does not need any further modification. It remains to treat the other terms of the right hand-side that we now call rhs :

$$rhs = \vec{\nabla} \cdot [s_e \tilde{h} - s_e e f + \rho s_\rho f] - \vec{\nabla} \cdot \tilde{h} \vec{\nabla} s_e - f \vec{\nabla} (e s_e) - f \vec{\nabla} (\rho s_\rho)$$

The first term of rhs is a conservative terms. By choosing carefully a definition for \tilde{h} and f , the conservative term can be expressed as a function of the entropy s . It is also required to include the variable area in the choice of the dissipative terms so that when assuming constant area, the regular multi-D Euler equations are recovered. The following definitions for \tilde{h} and f are chosen:

$$\tilde{h} = A\kappa\vec{\nabla}(\rho e) \text{ and } f = A\kappa\vec{\nabla}\rho,$$

which yields, using the chain rule:

$$rhs = \vec{\nabla} \cdot (A\kappa\vec{\nabla}s) - A\kappa \underbrace{\left[\vec{\nabla}(\rho e)\vec{\nabla}s_e + \vec{\nabla}\rho\vec{\nabla}(e s_e) + \vec{\nabla}(\rho s_\rho) \right]}_{\mathbf{Q}}$$

It remains to treat the term \mathbf{Q} that can be recast under a quadratic form, following the work done in [3]:

$$\begin{aligned} \mathbf{Q} &= X^t \Sigma X \\ \text{with } X &= \begin{bmatrix} \vec{\nabla}\rho \\ \vec{\nabla}e \end{bmatrix} \text{ and } \Sigma = \begin{bmatrix} \partial_\rho(\rho^2 \partial_\rho s) & \partial_{\rho,e}s \\ \partial_{\rho,e}s & \partial_{e,e}s \end{bmatrix} \end{aligned}$$

The matrix Σ is symmetric and identical to the matrix obtained in [3]. The sign of the quadratic form can be simply determined by studying the positiveness of the matrix Σ . In this particular case, it is required to prove that the matrix is negative definite: the quadratic form is in the right hand-side and is preceded of a negative sign. According to [3], the convexity of the opposite of the entropy function s with respect to the internal energy e and the specific volume $1/\rho$ is sufficient to ensure that the matrix Σ is negative definite.

Thus, the right hand-side of the entropy residual Eq. (28), are now either recast as conservative terms, or known to be positive. Following the work done by [3], the entropy minimum principle holds.